



HAL
open science

Fatigue performances of chemically etched thin struts built by selective electron beam melting: Experiments and predictions

Theo Persenot, Alexis Burr, Remy Dendievel, Jean-Yves Buffiere, Éric Maire, Joël Lachambre, Guilhem Martin

► To cite this version:

Theo Persenot, Alexis Burr, Remy Dendievel, Jean-Yves Buffiere, Éric Maire, et al.. Fatigue performances of chemically etched thin struts built by selective electron beam melting: Experiments and predictions. *Materialia*, 2020, 9, 10.1016/j.mtla.2020.100589 . hal-03367358

HAL Id: hal-03367358

<https://hal.science/hal-03367358>

Submitted on 21 Jul 2022

HAL is a multi-disciplinary open access archive for the deposit and dissemination of scientific research documents, whether they are published or not. The documents may come from teaching and research institutions in France or abroad, or from public or private research centers.

L'archive ouverte pluridisciplinaire **HAL**, est destinée au dépôt et à la diffusion de documents scientifiques de niveau recherche, publiés ou non, émanant des établissements d'enseignement et de recherche français ou étrangers, des laboratoires publics ou privés.



Distributed under a Creative Commons Attribution - NonCommercial 4.0 International License

Fatigue performances of chemically etched thin struts built by selective electron beam melting: experiments and predictions

Théo Persenot¹, Alexis Burr¹, Rémy Dendievel², Jean-Yves Buffière¹,
Eric Maire¹, Joël Lachambre¹, Guilhem Martin^{2#}

1. INSA Lyon, CNRS, MATEIS, F-69621 Villeurbanne, France
2. Univ. Grenoble Alpes, CNRS, Grenoble INP, SIMaP, F-38000 Grenoble, France

Corresponding Author: guilhem.martin@simap.grenoble-inp.fr

Abstract

Thin Ti-6-Al-4V tensile fatigue specimens were specifically designed to mimic struts of a lattice structure. Those samples were **subjected** to HIP and chemical etching that are thought suitable for complex geometries (machining was excluded). The effect of each post-treatment, as well as their combination on the fatigue performance is evaluated and quantified. Fatigue cracks are found to systematically initiate from surface defects. An original approach based on a full-3D non-destructive characterization by X-ray microtomography is developed to identify the population of those defects and rank them based on their size. *Kitagawa-Takahashi* diagrams are then used as a predictive tool regarding fatigue failure of samples containing defects. We show that ranking the defect size alone does not fully reflect the harmfulness of the identified defects.

Keywords: Additive Manufacturing; Ti-6Al-4V; Fatigue; Chemical etching; X-ray microtomography

1. Introduction

Manufacturing complex lattice structures has been made easier with the emergence of additive manufacturing processes, see e.g. [1–4]. Powder-bed techniques turn out to be the most efficient since they offer a lot of design freedoms [5]. It has been demonstrated that the mechanical properties of materials produced by such processes have mechanical properties that match the standards of wrought materials, see e.g. [6–8]. However, this was demonstrated based on bulk specimens that were preliminary machined from as-built samples. When considering as-built samples, the mechanical properties, in particular the fatigue performances are much lower than those of wrought materials [9–14]. This significant knock-down of the fatigue properties has been attributed to the presence of severe notch-like surface defects [11,13]. The density of those surface defects increases drastically in lattice structures and post-processing routes such as machining [6,7,10] or shot peening [15–18] can no longer be considered. Thus one has to apply alternative post-treatments to reduce the harmfulness of surface defects. Chemical etching can be applied to lattice structures [19,20][21,22]. This post-treatment helps to decrease the density of surface defects and it also enables to reduce the harmfulness of surface notch-like defects [19]. Because of the relatively small diameter of the lattice struts, erasing all

surface defects in a lattice structure is not possible. Thus such structures will always contain surface defects and, therefore, a theoretical framework is required to deal with those defects.

In the present work, to mimic the behavior of thin parts or struts, thin tensile Ti-6Al-4V fatigue specimens were built by selective electron beam melting (S-EBM). Those samples can be considered as representative of struts in any stretching dominated lattice structure where the predominant loading modes are uniaxial tension and compression. As a consequence, the results of the present investigation provide insights into the fatigue performance of individual struts in a stretching dominated lattice structure. Note that from the present work, we cannot draw conclusions for the case of bending dominated lattice structures. The effect of various post-treatments: HIP, chemical etching or a combination of both on the fatigue properties of those struts is evaluated. We developed a methodology based on X-ray microtomography to identify the population of the defects leading to fatigue failure relying on the \sqrt{area} parameter introduced by Murakami *et al.* [23][24]. As a result, each defect can be reported on Kitagawa-Takahashi diagrams and fatigue failure can be predicted. The validity of those diagrams is also discussed.

2. Experimental Procedures

2.1. Material and sample geometry

Cylindrical tensile specimens with a gauge length of 10 mm and a nominal diameter of 2 mm were produced with three different orientations with respect to the building direction: horizontal, vertical and 45°-tilted specimens, using an ARCAM A1 EBM machine loaded with Ti-6Al-4V ELI powder. The chemical composition of the initial powder batch is given in **Table 1**. It has been demonstrated that the build orientation has an impact on the fatigue properties, see e.g. [10,13]. In the present work, only struts produced vertically with their axis parallel to the building direction were selected to further evaluate the impact of post-treatments. The relatively small nominal diameter (2 mm) was deliberately chosen so as to be representative of a single strut of a lattice structure or a thin part [25]. The standard "Melt" build theme recommended by ARCAM for a layer thickness of 50 μm was chosen to define the set of melting parameters and scanning strategy used during the EBM process. Details regarding the melting strategy can be found in [13][25].

Elements	Al	V	C	Fe	O	N	H	Ti
wt.%	6.47	3.93	0.01	0.22	0.09	0.01	0.001	Bal.

Table 1. Chemical composition of the initial Ti-6Al-4V powder batch used for this investigation.

2.2. Post-treatments

Two types of post-treatments were applied to the as-built fatigue specimens:

(i) Hot Isostatic Pressing (HIP) was used to reduce the amount of internal defects, like lack of fusion defects or gas pores inherited from the initial powder (entrapped gas during the atomization process). Here the following conditions were used: annealing of 2h at 920°C under

a pressure of 1000 bar immediately followed by a slow furnace cooling (standard conditions used by the aeronautic industry for HIPing components fabricated by conventional powder metallurgy processing routes and made of the Ti-6Al-4V Ti-alloy).

(ii) Chemical etching (CE) was employed to decrease the surface defects severity of the as-built fatigue specimens. Each specimen was dipped at room temperature in a fresh solution consisting of 12 mL HF (48%), 40 mL HNO₃ and 300 mL of distilled water (no stirring of the solution) for 45 min [19,20,25]. The specimens were rinsed under water immediately after being removed from the etchant in order to avoid any residual contamination of acid.

Each of those post-treatments was applied separately or in combination (HIP followed by chemical etching).

2.3. Fatigue testing

Constant amplitude stress controlled uni-axial tests were carried out with a frequency $f = 10$ Hz (sinusoidal wave form) and a stress ratio $R = 0.1$ at room temperature using a servo-hydraulic INSTRON 8516 fatigue testing machine equipped with a 5kN cell force.

In the as-built conditions, the sample cross sections can vary significantly along the gauge length, see [25,26]. Therefore, the cyclic stresses were calculated based on the *average section* along the gauge length determined from the tomographic scans. This definition was found to be more suitable for stress calculation in this type of samples [13,25]. The fatigue tests were performed until failure or stopped after at least 10^6 cycles (run outs).

2.4. Material characterization

The gauge length of the fatigue samples was fully characterized using laboratory X-ray tomography. The fatigue specimens were inspected in the as-built conditions as well as after different post-treatments with a cone beam phoenix | x-ray V | tome | x-laboratory tomograph using a 2.5 μm voxel size (spatial resolution of ≈ 4 μm). Systematic inspections were also performed after fatigue failure. Detailed information on the setup can be found in [13]. The following scanning parameters were used: voltage $V=90$ kV, current $I=240$ μA , exposure time= 333 ms, 720 projections per scan. No filter was needed. Five scans were required to image the whole gauge length. The scanning time per sample was roughly 1h. The reconstruction of the 3D images was performed using a standard filtered back projection algorithm (phoenix datos x software). The reconstructed volumes were analyzed using Fiji software.

After fatigue failure, the fracture surfaces were inspected by SEM under secondary electron (SE) contrast.

3. Results and Discussion

3.1. S-N curves

The S-N curves of vertically built samples **subjected** to different post-treatments are shown in **Figure 1**. Note that S-N curves have been plotted using respectively the stress range (**Figure 1a**) and the maximum stress (**Figure 1b**). Plotting the S-N curve with the stress range

will be useful in section 5 dealing with fatigue failure predictions, in particular when plotting Kitagawa-Takahashi diagrams. Results from the literature for machined and HIP+machined samples built by EBM are used for comparison [6,10,27].

As discussed in [13], those curves are well below the S-N curve determined in [27] for machined samples because of the presence of numerous notch-like surface defects which systematically lead to crack initiation. However, after chemical etching, a clear improvement of the fatigue properties is observed, see **Figure 1a**. Both the fatigue limit (taken at 10^7 cycles) and the fatigue resistance at 10^5 cycles are enhanced by nearly 75 MPa compared to the as-built limit. This corresponds to an enhancement of roughly 50% for the fatigue limit and about 30% for the fatigue resistance at 10^5 cycles. Interestingly, the scattering of the data is substantially increased when chemical etching is applied when compared to as-built conditions. No beneficial effect of a sole HIP-treatment was detected, because fatigue failure is driven by surface defects as discussed in [13]. When samples are **subjected** to HIP prior to chemical etching, fatigue performances are further improved. In the as-built conditions, samples break at 10^5 cycles under a maximum stress of roughly 210 MPa while they can sustain a maximum stress of about 360 MPa after HIP+chemical etching, see **Figure 1b**. Similarly, the fatigue limit is increased by nearly 100% when using a combination of HIP and chemical etching in comparison to as-built conditions, see **Figure 1**.

3.2. Fracture surface and identification of the killer defect

In order to identify the defect that leads to the final failure (“killer defect”) within the population of the surface defects in the sample gauge length, repeated tomographic scans were performed before and after failure, as explained in [13]. **Note that the terminology killer defect has been used to describe the most detrimental defect in additively manufactured components, see e.g. [28,29].** This enables to determine at which slice in the tomographic reconstruction along the gauge length, fatigue failure occurs. From this slice and from the SEM image of the fracture surface, the killer defect can be unambiguously identified (see for example **Figure 2a-e**). Its geometry (size and shape) can be determined based on the tomographic images before fatigue testing, see **Figure 2c-e**. Note that, in this example, the morphology of the killer defect observed on the fracture surface matches relatively well with the one determined on the corresponding 2D-tomographic slice, see comparison between **Figure 2b** and **Figure 2e**.

A similar analysis of all the fracture surfaces demonstrates that for chemically etched samples the crack leading to failure initiates and propagates systematically from the surface defects left by chemical etching as shown in **Figure 2a**. An enlarged view of the surface defect is given in **Figure 2b**. The same observation is made for samples **subjected** to HIP before chemical etching. Internal pores are never found at the origin of the crack leading to fatigue failure.

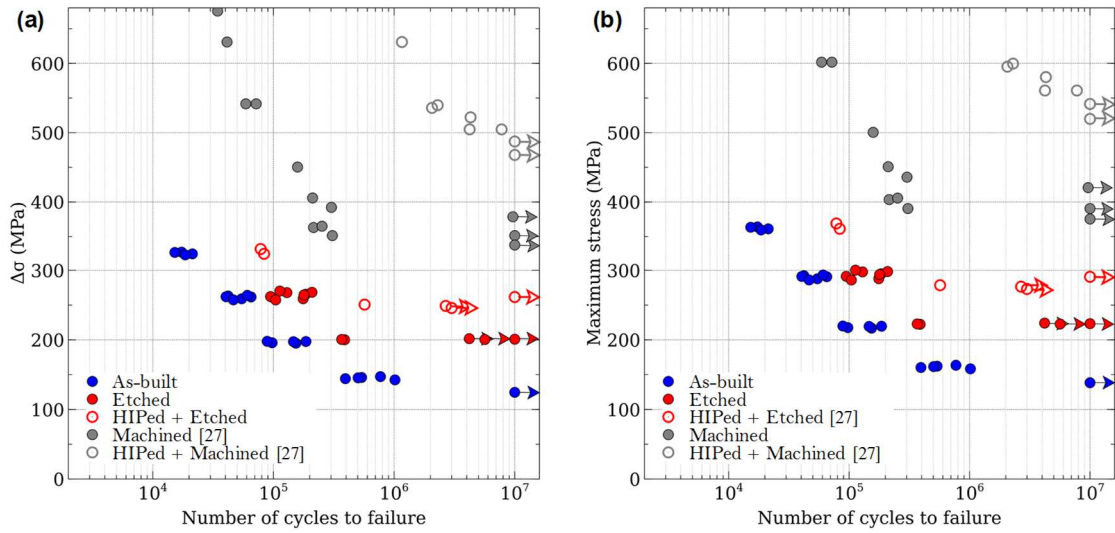


Figure 1. (a) S-N curves for EBM fatigue samples built vertically plotted using the stress range $\Delta\sigma$ and (b) plotted using the maximum stress. The gray (extracted from [27]), red and blue dots depict respectively the machined, chemically etched and as-built conditions. Hollow symbols stand for samples for which HIP was applied. The data on machined samples was obtained from ARCAM [27].

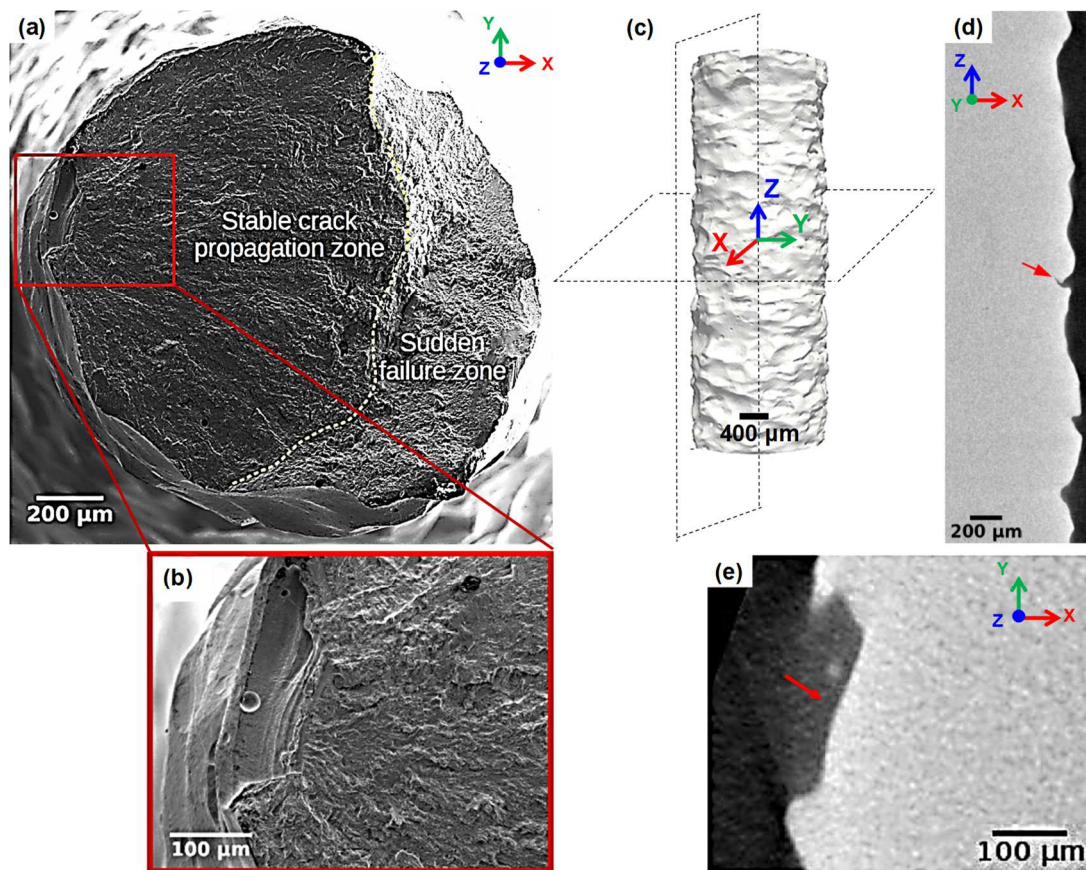


Figure 2. (a) SEM-SE micrograph of the fracture surface of a chemically etched sample after fatigue failure showing the stable crack growth and sudden failure zones. (b) Higher magnification SEM-SE micrograph showing the crack initiation site. (c) 3D reconstruction from X-ray microtomography of a sample subjected to chemical etching before fatigue testing. 2D cross sections obtained by X-ray tomography showing the morphology of the killer defect (red arrow) before fatigue testing: (d) in the (XZ)-plane and (e) in the (XY)-plane. Z-direction corresponds to the building direction while (X, Y) directions define the building plane.

3.3. Rationalization of the enhancement of the fatigue properties with post-treatments

3.3.1. Chemical etching

Chemical etching brought **an improvement** of the fatigue properties in comparison with as-built conditions whether or not the samples are HIPed beforehand. However, the fatigue properties still suffer from a significant knock-down when compared to machined samples. Moreover, chemical etching adds a substantial scatter to the number of cycles to failure, see **Figure 1**. Fatigue failure systematically initiates from a surface defect. The latter observation is consistent with the fact that for samples only **subjected** to chemical etching, failure **does not occur** due to an internal defect. **Note that over all the samples investigated in the present work, none of them failed under cyclic loading due to an internal defect.**

The effect of chemical etching on the fatigue performance of EBM built parts has been investigated using tomographic scans performed before and after chemical etching. To better reflect the impact of chemical etching, 2D reconstructed slices before (dark gray) and after (light gray) chemical etching are superimposed on **Figure 3a-d**. It can be seen in this figure that the as-built surface defects are smoothed during chemical etching but not totally erased since deep notch-like defects remain. Sometimes chemical dissolution leads to shallow defects, see typically green arrows in **Figure 3a**. Interestingly, the harmfulness of the deep notch-like defects observed in the as-built samples is reduced: their depth is decreased and the radius of curvature at their root is increased, see e.g. defects pointed out by red arrows in **Figure 3a-d**. The killer defect was always found among those residual notch-like defects, except in a case where it was an internal defect brought to the surface by chemical etching, see e.g. **Figure 3e-f**. Note that such a peculiar situation can be solved with a preliminary HIP treatment. Microtomography scans performed before and after chemical etching provides insights into the evolution of the notch-like surface defects observed in the as-built conditions and give a sound explanation to the fatigue enhancement brought by chemical etching.

3.3.2. Effect of a preliminary HIP treatment

HIP seems to clearly have a beneficial effect on the fatigue performances when combined to chemical etching. At first sight, this can be considered as contradictory with the results reported in [10,13] where it was shown that HIP had no effect on the fatigue performance as long as as-built surface with notch-like defects are considered. Here, instead it was found that performing HIP prior to chemical etching improves the fatigue limit of the etched samples. This could be first related to a change of the killer defect morphology. However, this is unlikely to be the case since very similar surface defects are observed in chemically etched samples whether or not they were HIPed beforehand. The enhancement of the fatigue properties brought by HIP prior to chemical etching could also be linked to a change of material properties, in particular of crack growth mechanisms near the threshold region. For a stress ratio $R = 0.1$, the crack growth parameters of EBM as-built machined [6,30–34], and HIPed and machined [6,30–33] Ti-6Al-4V samples have been determined through standard fatigue crack growth tests. Comparing the crack growth parameters of as-built and HIPed samples help to appreciate how the coarsening of the alpha laths induced by HIP affects the crack growth of EBM samples, see e.g. **Table 2**. Greitmeier *et al.* [30] and Seifi *et al.* [32,33] report a crack growth threshold (ΔK_{th}

MPa \sqrt{m}) higher for samples **subjected** to HIP. In other words, samples exhibit a better crack propagation resistance when HIP is applied. Galaraga et al. [34] also reported an increase of the fatigue crack growth threshold after a heat treatment at 1100°C for 30 minutes followed by a slow cooling rate which had induced a substantial coarsening of the microstructure. In our case, therefore, the improvement of the fatigue performances when HIP is applied prior to chemical etching could be attributed to the coarsening of the microstructure occurring during HIP operations which makes the samples more resistant to fatigue crack propagation [34]. To summarize, decreasing the surface defect harmfulness through chemical etching and increasing the fatigue crack growth resistance through HIPing (coarser microstructure), lead to a considerable enhancement of the fatigue performances of as-built samples produced by EBM. However, when only HIP is applied, its beneficial effect in the threshold region is completely erased by the harmfulness of the surface defects.

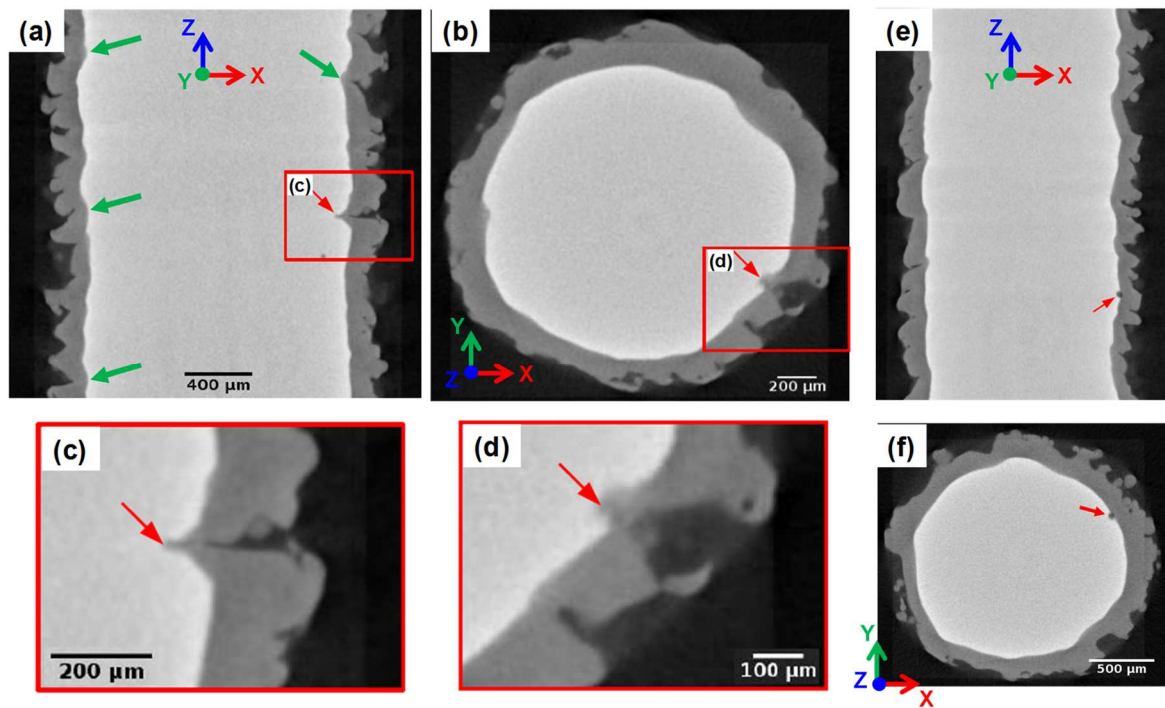


Figure 3. (a)-(d) Overlay of 2D reconstructed images of the gauge length of a fatigue sample; as-built (dark gray) and after chemical etching (light gray) in both (XZ)-plane (see (a) and (c)) and (XY)-plane (see (b) and (d)). The very irregular as-built surface is substantially smoothed due to chemical etching but deep defects remain, see typically red arrows in (a), (b), (c) and (d). Green arrows in (a) show shallow defects with a large radius of curvature. (e) (XZ)-view and (f) (XY)-view showing an internal pore (red arrow) brought to the surface after chemical etching.

Reference	Condition	Stress ratio, R	Crack growth orientation	ΔK_{th} (MPa \sqrt{m})
[30]	As-built+machined	0.1	unknown	4.2
	HIP+machined	0.1	unknown	4.8
[33]	As-built+machined	0.1	Normal to the building direction (BD)	4.0
	HIP+machined	0.1	Normal to the building direction (BD)	5.1
[34]	As-built+machined	0.1	Normal to the building direction (BD)	3.8

Table 2. Summary of the fatigue crack growth thresholds ΔK_{th} found in the literature [30,32] for Ti-6Al-4V produced by EBM and for cracks propagating perpendicularly to the building direction.

4. Systematic detection of the deepest surface defects

We have shown that the killer defect under cyclic loading is systematically a surface defect with a notch-like morphology. Thus, in order to predict fatigue failure of chemically etched samples, a methodology allowing a systematic detection through non-destructive inspections of the most harmful surface defects prior to fatigue testing is needed. We suggest to detect those harmful defects relying on the significant local variations that they induce on the distance r between the central axis and the surface as defined in **Figure 4a**.

4.1. Binarization and “unfolding” of the surface

Grayscale X-ray tomography 3D images of the gauge length are first transformed into binary images through thresholding. Internal defects (typically for samples not **subjected** to HIP) are suppressed using a 3D objects detection method immediately followed by hole filling. The 3D volume is then resliced to produce radial reconstructions of the stack of the sample sections, see **Figure 4b**. The latter process leads to the “unfolding” of the surface as shown in **Figure 4c**. The radial step $d\theta$ is determined so that the voxels at the external surface of the sample are not distorted and keep their cubic-shape with a size of $2.5\ \mu\text{m}$. The result of those operations is a new 3D image which X, Y and Z axes correspond to the r , θ and Z parameters of the initial volume.

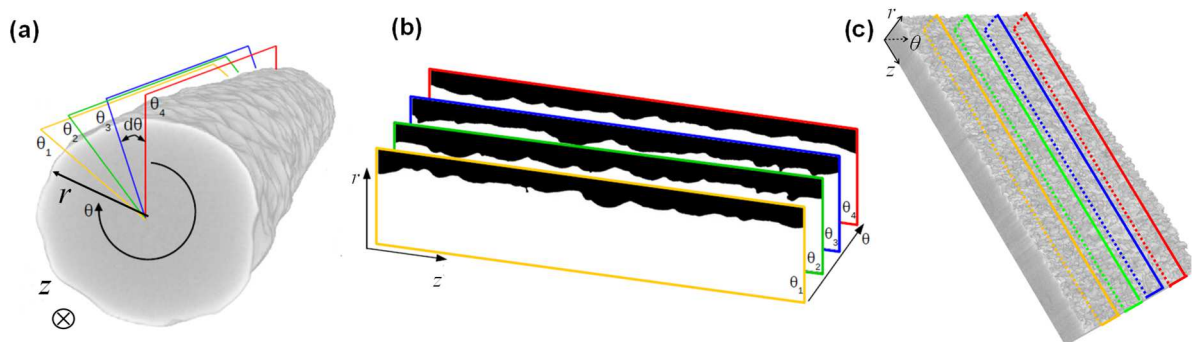


Figure 4. Schematic illustration of the “unfolding” and reslicing process where radial slices are produced from the stack of the 3D reconstructed sections. (a) A line starting from the sample central axis and ending at the edge of the tomographic image is rotated around its starting point with a radial step $d\theta$. (b) Examples of tomographic 2D projections after binarization and reslicing. (c) 3D view of the reconstructed surface subsequently to the “unfolding process”.

4.2. Local height calculation

As detailed in **Figure 5**, the distance of every surface voxel to the central axis, can be computed by summing the voxels along the r direction, a voxel of material counting for 1 while a voxel of void counts for 0, see **Figure 5a**. As a result, a scalar value is obtained for every (Z, θ) coordinates within the image and corresponds to a given height. This set of calculated heights is used to produce a 2D grayscale image (see **Figure 5b**) which is a map of the distance between the surface and the sample central axis. Dark gray areas correspond to short distances, i.e. significant intrusions and light gray areas correspond to longer distances, i.e. large protrusions. An example of such a map is given in **Figure 5b**. The radial step $d\theta$ being constant along the sample radius, the voxels located close to the sample central axis are distorted radially.

However, the latter drawback does not matter since the methodology mainly relies on the voxels located in the vicinity of the surface, region where notch-like defects are located. Note also from the observation of **Figure 5b** that the distance to the center exhibits variations at different ranges. Short range variations are caused by surface roughness induced by the EBM process, including unmelted attached powder particles and plate-pile like defects. Long range variations (note for instance the two dark vertical bands in **Figure 5b** caused by geometrical macroscopic imperfections of the specimen section).

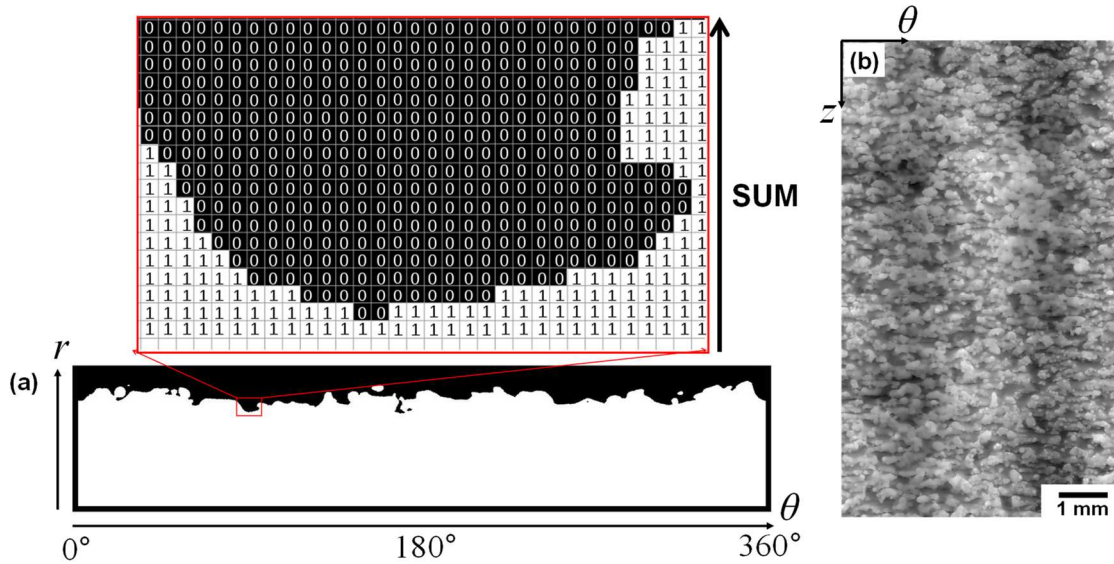


Figure 5. (a) Schematic illustrating the calculation of the distance between the central axis and every voxel belonging to the surface. (b) Unfolded surface: each pixel represents a physical point P at the sample surface, with a gray value equal to the distance between P and the sample center.

4.3. Identification of the deepest notch-like defects

Those grayscale surface maps need additional image processing steps in order to identify only the lowest height values corresponding to the deepest and sharpest notch-like surface defects and to exclude from the analysis smooth surface height variations. Shallow defects left by chemical etching (green arrows in **Figure 3a**) should be excluded as they induce only a slight stress concentration. In particular, long and middle variations of the distance to the center has to be subtracted to allow the detection of very short range variations, representative of notch-like defects. In order to do so, a Gaussian blur operation is applied to the initial unfolded grayscale surface map. This filter uses a Gaussian convolution function to smooth the grayscale variations within the grayscale map. A radius R defines the size of the disc used in the Gaussian function calculation, here $R = 50 \mu\text{m}$ was used. The result of this operation on a notch-like defect as well as on a smooth surface defect are illustrated respectively in **Figure 6a** and **Figure 6b** representing profiles of the measured distance r along the axis of the strut. The grayscale surface map obtained after the filtering process (**Figure 6d**) can be subsequently subtracted to the initial grayscale surface map (**Figure 6c**) so that only the *local* surface height variations are revealed, see **Figure 6e**. The new grayscale surface map shows the local height variations, i.e. the difference between the local height value and the average one calculated from the blurred grayscale surface map. Protrusions and extrusions are respectively shown by positive and

negative values. The lowest values, associated to dark areas, hence correspond to the deepest notch like defects. The population of the deepest surface notch-like defects is finally obtained through a last thresholding of the final grayscale surface map, see **Figure 7a-b**). The thresholding value TS needs to be optimized in order to retain only the population of deep notch-like defects. After a few trials, a value of $TS = 60 \mu\text{m}$ was observed to be appropriate to select the targeted defects. A full-detailed description of the relatively complex optimization procedure for determining TS and R is not provided here as it was considered out of the scope of the present contribution, the details can be found in [35] .

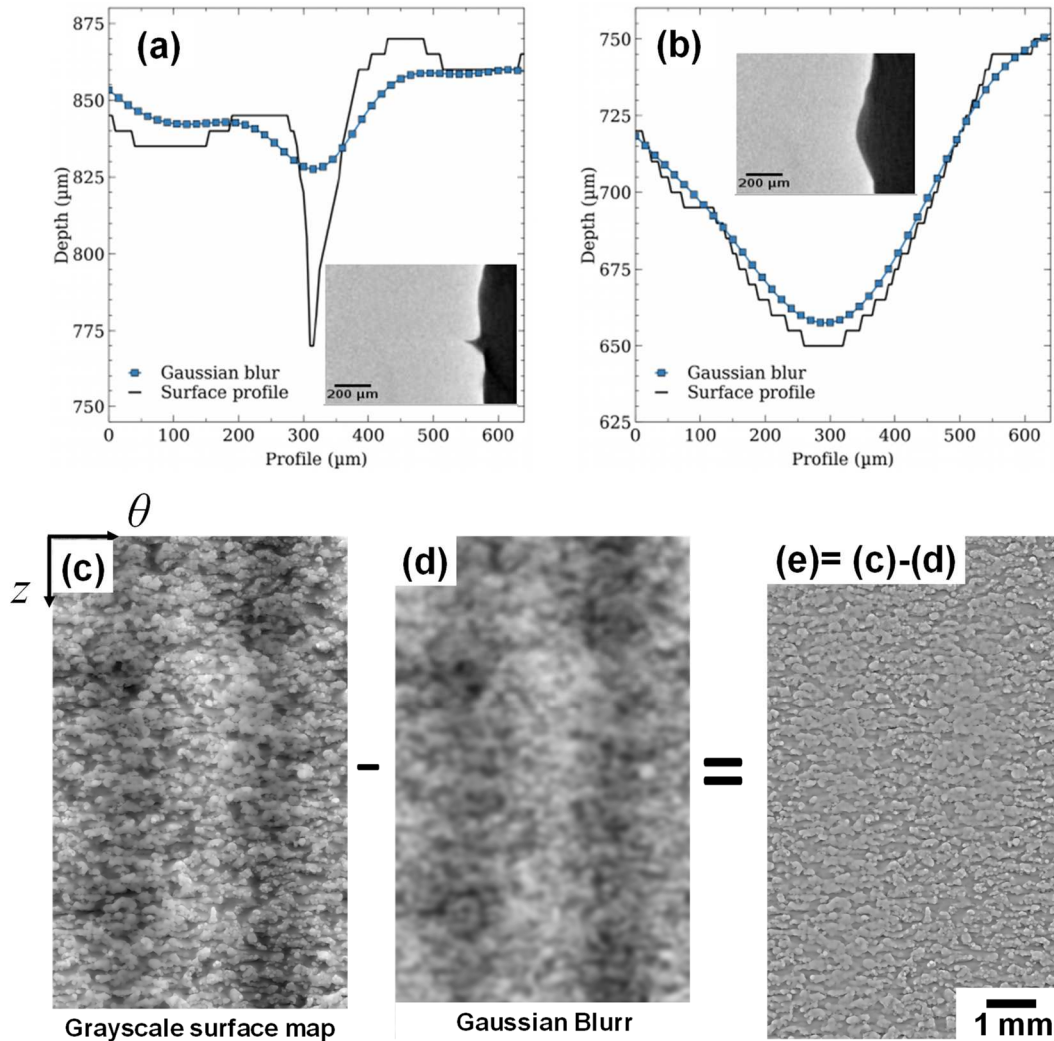


Figure 6. Illustration of the effect of the Gaussian blur on the surface profiles of a notch-like defect (a) and on a smooth stacking irregularity (b). The resulting profiles are represented by blue lines with square symbols while the as-built surface profiles are shown by black solid lines. (c) Initial grayscale surface map where the grayscale level corresponds to the distance between the surface and the center of the sample. (d) Gaussian blurring of this initial grayscale surface map. (e) Grayscale surface map resulting from a mathematical subtraction of images (c) and (d) (i.e. (c)-(d)) and allowing to exclude from the analysis smooth height variations that do not correspond to deep notch-like defects. These maps show the entire sample gauge length ($\approx 5.8 \text{ mm}$ perimeter and 10 mm height).

4.4. Validation

The methodology developed to identify automatically the deepest surface notch-like defects has been validated in order to make sure that it efficiently captures the population of the deepest notch-like defects as shown in **Figure 7**.

The surface defects identified after thresholding (**Figure 7b**) are visually compared with those present in the 3D initial images of the sample gauge length. As shown in **Figure 7b** and **Figure 7c**, all thresholded defects do correspond to surface defects which can be expected (again based on visual inspection) to produce a stress raiser effect. Besides, the killer defect identified as illustrated in **Figure 2** is also clearly detected. The same results were obtained on several samples and therefore give us confidence in the ability of the proposed method to identify the population of potentially harmful defects. Note that in this validation procedure we relied on the defect depth in order to identify the population of harmful defects but in the subsequent analysis, the defect size taken as the root square of the projected area (\sqrt{area}) as initially suggested by Murakami [23,24] will be used.

The current approach to identify the population of the most harmful surface defects based on a 3D non-destructive characterization was applied to samples built by selective electron beam melting. However, we would like to highlight that this methodology can be applicable to samples fabricated by other AM processing routes that generate many surface defects, in particular to the more popular Laser Powder Bed Fusion (L-PBF).

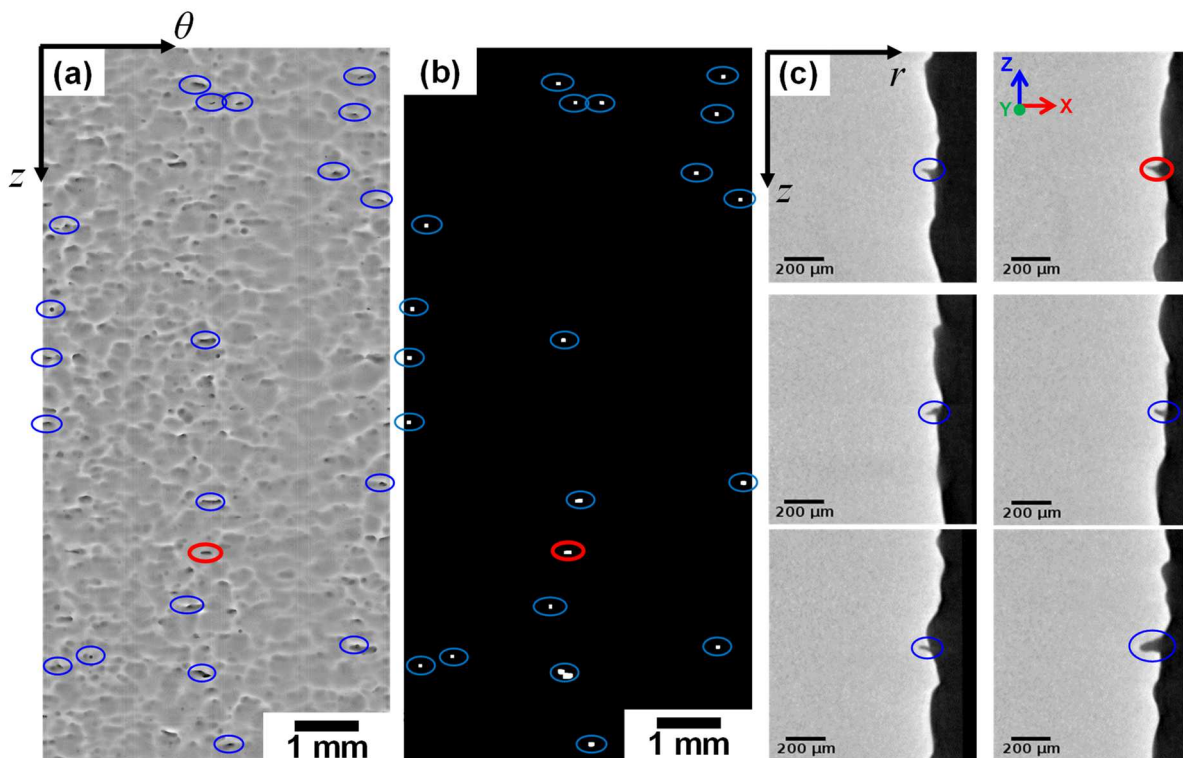


Figure 7. Validation of the automated detection of the deepest notch like defects illustrated based on an example of a chemically etched sample. (a) Grayscale surface map after all processing steps. (b) Thresholding of (a) to identify the deepest notch like defects, highlighted in blue in (a) and reported in (b). (c) 2D-cross sections of the reconstructed volume in the (XZ)-plane showing examples of several identified defects using our detection method (encircled in blue). The killer defect identified through the methodology illustrated in **Figure 2** is encircled in red.

5. Predictions of fatigue failure of chemically etched specimens

5.1. Classical Kitagawa-Takahashi diagrams

Murakami [23,24] has shown that, from the view point of fatigue, defects such as intermetallic particles, surface cavities or pores can be considered equivalent to cracks with a stress intensity factor range that can be written as follows:

$$\Delta K = Y\Delta\sigma\sqrt{\pi\sqrt{area}}, \quad (1)$$

where Y is a dimensionless factor which depends on crack location (typically 0.65 for a surface crack and 0.5 for an internal defect), $\Delta\sigma$ is the stress range, and \sqrt{area} the square root of the defect area projected in a direction normal to the applied stress.

The *Kitagawa-Takahashi* diagram can be used to link the fatigue limit of a given specimen to the size of the defects that it contains [36]. To build such a diagram, two fatigue parameters are needed: (i) the classical fatigue limit, σ_f and (ii) the crack growth threshold, ΔK_{th} in order to establish the non-propagation conditions for cracks. The value of σ_f is determined using a S-N curve obtained with defect-free samples and is used as the non-propagation condition for short cracks. ΔK_{th} corresponds to the stress intensity range below which long cracks do not propagate. The equation of the curve delimitating the region of non-crack propagation from the region where cracks can grow is given by equation (2).

$$\Delta\sigma_{lim} = \min\left(\Delta\sigma_f, \frac{\Delta K_{th}}{Y \cdot \sqrt{\pi\sqrt{area}}}\right) \quad (2)$$

$\Delta\sigma_f$ is the stress amplitude taken at the fatigue limit σ_f . Thus two straight lines can be drawn for respectively both short and long cracks regimes in a log-log plot. In order to determine a smooth transition between the short and long crack propagation regimes, El Haddad *et al.* [37]

conducted experimental studies and defined a defect size $\sqrt{area_0} = \frac{1}{\pi} \cdot \left(\frac{\Delta K_{th}}{Y\Delta\sigma_f}\right)^2$. For defect

smaller than that size, the fatigue threshold no longer depends on the defect size and a single empirical equation allows to fully describe the curve $\Delta\sigma_{lim} = f(\sqrt{area})$:

$$\Delta\sigma_{lim}^{ElHaddad} = \frac{\Delta K_{th}}{Y \cdot \sqrt{\pi(\sqrt{area} + \sqrt{area_0})}}. \quad (3)$$

The fatigue failure of etched samples being always caused by surface defects, in this work, machined samples are considered as defect-free samples. The fatigue limits σ_f taken at 10^7 cycles of respectively machined ($\sigma_f = 380-400$ MPa) and HIPed+machined ($\sigma_f = 500-520$ MPa) samples and reported in [27] are used. Those values can be directly extracted from **Figure 1**. Results of standard fatigue crack growth tests performed on Ti-6Al-4V built by EBM published in [30–33,38] are used for the crack growth threshold, ΔK_{th} . The average value of ΔK_{th} as well as both minimum and maximum values are used to build the *Kitagawa-Takahashi* diagram shown in **Figure 8** in order to better reflect the scattering of the literature data, see e.g. **Table 2**.

The defect harmfulness is evaluated through the square root of the projected area of the defect (\sqrt{area}) as initially suggested by Murakami *et al.* [39] and recently proposed in the framework of additive manufacturing, see e.g. [9,11,40]. For every defect within the population obtained with our methodology, the \sqrt{area} parameter is measured using microtomography images. Both local minimum and maximum projections of the microtomography images along the loading axis are superimposed to determine the exact projected area of the defect, see an illustration of the methodology provided as supplementary materials in **Figure S1**. This experimental data is used to build the *Kitagawa-Takahashi* diagrams in order to predict the fatigue failure. The sizes and square root values of the projected areas of all defects detected in a given specimen is shown as supplementary materials in **Figure S2**.

Overall, 19 fatigue specimens have been analyzed with the developed methodology for the *R* and *TS* values optimized. The number of deep surface defects per fatigue specimen identified through our methodology is about 15 on average. It means that in total nearly 300 surface defects have been examined and inserted on the *Kitagawa* diagrams shown in **Figure 8**. Note that if the detection method of the residual notch-like defects was automatic, the determination of the projected area was performed manually making difficult to evaluate a much larger population of defects. For the sake of clarity, four *Kitagawa-Takahashi* diagrams are plotted in **Figure 8** in order to differentiate:

- unbroken (run outs, $N > 10^6$ cycles) (**Figure 8a** and **Figure 8c**) from broken (**Figure 8b** and **Figure 8d**) specimens (failure occurring between $8 \cdot 10^4$ and $6 \cdot 10^5$ cycles);
- non-HIPed ((**Figure 8a** and **Figure 8b**) from HIPed samples (**Figure 8c** and **Figure 8d**).

For all unbroken samples (6 samples in total: 3 **subjected** to HIP+chemical etching and 3 **subjected** only to chemical etching), all the defects identified through our methodology stand in the safe region of the diagram, i.e. below the $\Delta\sigma_{lim} = f(\sqrt{area})$ curve in **Figure 8a** and **Figure 8c**. None of these defects is expected to induce crack growth at these stresses. As none of these samples broke during the experimental fatigue tests, it can be concluded that their fatigue failure is consistent with the *Kitagawa* framework whether or not the samples are HIPed beforehand.

Regarding broken samples (13 samples in total with failure occurring between $8 \cdot 10^4$ and $6 \cdot 10^5$ cycles), the killer defect (red dots in **Figure 8b** and **Figure 8d**) is located above the propagation curve for 11 samples meaning that sample fatigue failure is relatively well-predicted. Overall, out of the 19 chemically etched samples (with or without HIP), the fatigue behavior of 17 samples is correctly predicted by the classical *Kitagawa-Takahashi* diagrams. However, two cases are not correctly predicted since the killer defect stands below the propagation curve. Those predictions will be thoroughly discussed in the next section.

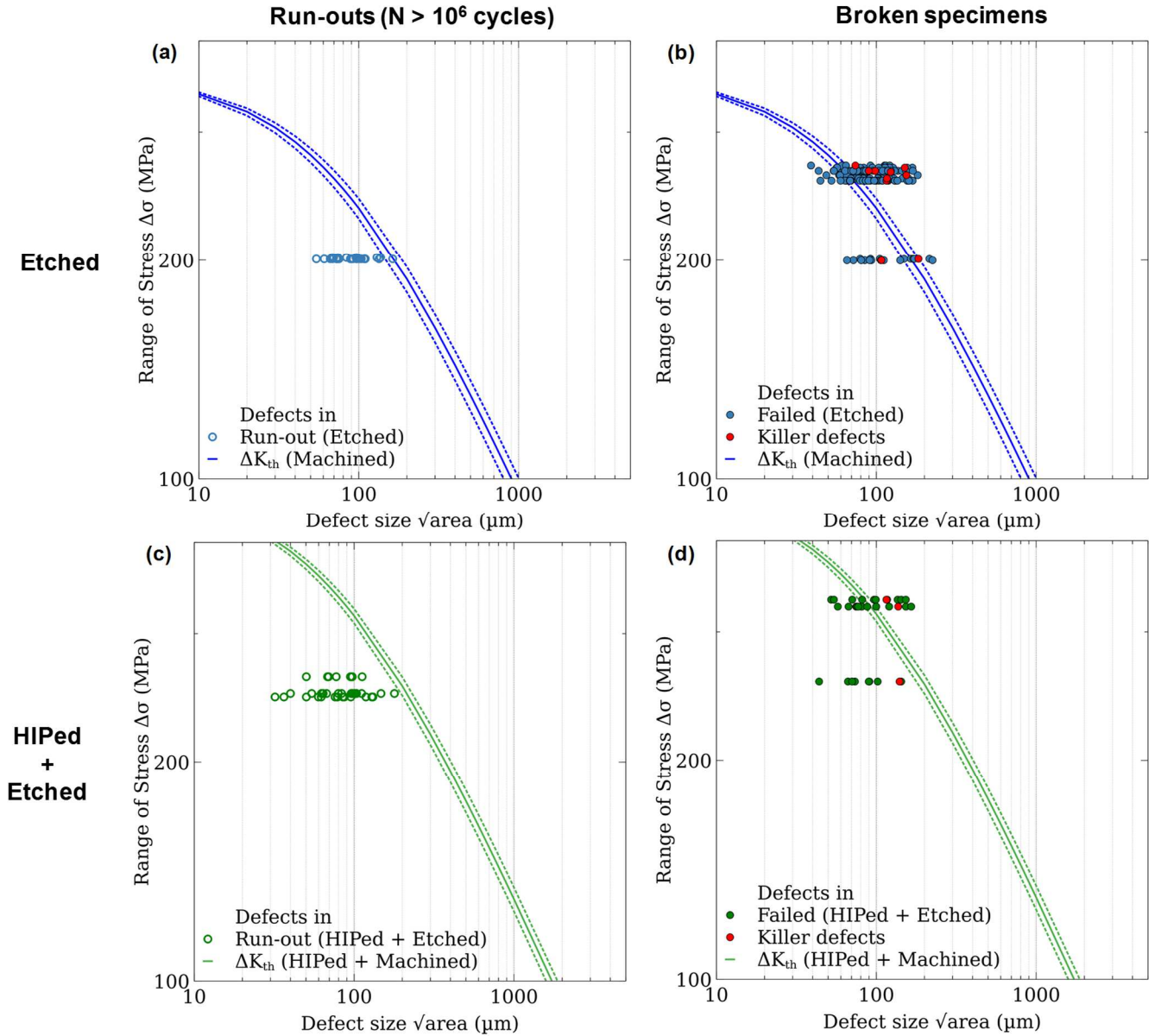


Figure 8. Kitagawa-Takahashi diagrams of chemically etched 90° samples. The blue (a,b) and green (c,d) colors correspond respectively to samples that did and did not undergo a HIP treatment. The continuous lines were plotted using the average ΔK_{th} value from the literature while minimum and maximum values were considered for the dashed lines. Each dot corresponds to a surface defect detected on the thresholded final surface maps and for which a projected area was estimated. Empty (a,c) and filled dots (b,d) stand for defect within respectively run-outs and failed specimens. The red dots represent the killer defects in the failed samples. The defect size defined as \sqrt{area} is measured on tomographic images.

5.2. Limits of the Kitagawa-Takahashi diagrams

5.2.1. Infinite vs. Finite fatigue lives

Regarding the use of the classical Kitagawa-Takahashi diagrams, one must be very careful to be consistent with the theoretical framework. Only samples tested at low stresses, i.e. having fatigue lives long enough to be close to the fatigue limit, can be directly reported. The fatigue limit is usually defined for a given number of cycles to failure (typically 10^7 cycles). Performing fatigue tests to achieve a given number of cycles is not possible. Therefore, in the literature, samples having survived at least the knee point of the S-N curve are usually considered and can

be directly reported on the *Kitagawa-Takahashi* diagrams, see e.g. [40] and [41]. This method is justified by the fact that in the high-cycle fatigue regime, the error on the load which has to be applied to reach a given fatigue life is significantly decreased. In addition, the crack growth rate is small enough to comply with the crack propagation close to the threshold, see [41] for a more detailed discussion. The consequence is that any data point tested at a maximum stress higher than the knee point of the S-N curve should not be directly inserted in a classical *Kitagawa-Takahashi* diagram.

In the present case, **Figure 1** shows that the knee region of the S-N curves of chemically etched samples with or without HIP corresponds to a number of cycles of the order of 2 to $4 \cdot 10^5$ cycles. Some data points in the S-N curve exhibit fatigue lives of the order or shorter than 10^5 cycles. Those data points should not be inserted in the classical *Kitagawa-Takahashi* diagrams shown in **Figure 8b** and **Figure 8d** or at least have to be considered carefully. Some authors have suggested different approaches to overcome this issue and to extend *Kitagawa* diagrams to finite lives, see [40] and [41]. The approach of Beretta and Romano [40] suggests to extrapolate fatigue lives shorter than the knee point of the S-N curve to larger fatigue lives, typically the one of the knee point region. The second approach proposed by Ciaravella *et al.* in [41] consists in extending the *Kitagawa* diagrams to finite fatigue lives. In this approach, the propagation curve has to be modified on both the right and left sides of the knee point of the $\Delta\sigma_{\text{lim}} = f(\sqrt{\text{area}})$ curve. The left part is given by the fatigue limit, defined as the stress range associated to a finite fatigue life in the S-N curve of machined samples. For the right part, a propagation law in the Paris regime is assumed and integrated for the desired finite fatigue life. We have attempted to apply both approaches [35]. The predictions using the modified approaches systematically show that all the defects including the killer defect lie below the propagation curves, and therefore should not propagate. From this it was concluded that classical *Kitagawa* diagrams give the best predictions since over the 19 samples examined, 17 are correctly predicted whereas modified approaches do not allow to predict the fatigue failure.

The fact that the classical *Kitagawa* diagrams give the best predictions for broken samples that have fatigue lives shorter than the knee-point above of the S-N curve should be briefly discussed. First, the exact position of the knee-point in our S-N curves of chemically etched samples might suffer from a substantial uncertainty given the limited number of samples analyzed, in particular for the samples **subjected** to HIP prior to chemical etching. Second, we should also raise that some samples that we have considered in our analysis were certainly tested at stresses slightly above the knee-point but were still tested at relatively low stress levels, i.e. relatively close to the knee-point stress value.

5.2.2. Ranking defect based on $\sqrt{\text{area}}$

Interestingly, the killer defect is hardly ever the one having the largest projected area, see **Figure 9** but is consistently identified as a notch-like defects, see several examples in **Figure S3**. In other words, it means that the $\sqrt{\text{area}}$ parameter seems to be insufficient to evaluate the harmfulness of a given surface defect. The morphology of the killer defects was investigated for all broken specimens and compared to that of the largest defect detected by the methodology. An example is provided in **Figure 10** where the surface defect responsible for

the fatigue failure (**Figure 10a-b**) is compared to the surface defect exhibiting the largest square root of the projected area (**Figure 10c-d**). Here the killer defect has a \sqrt{area} value equal to 90 μm while the largest defect detected shows a \sqrt{area} value of nearly 170 μm .

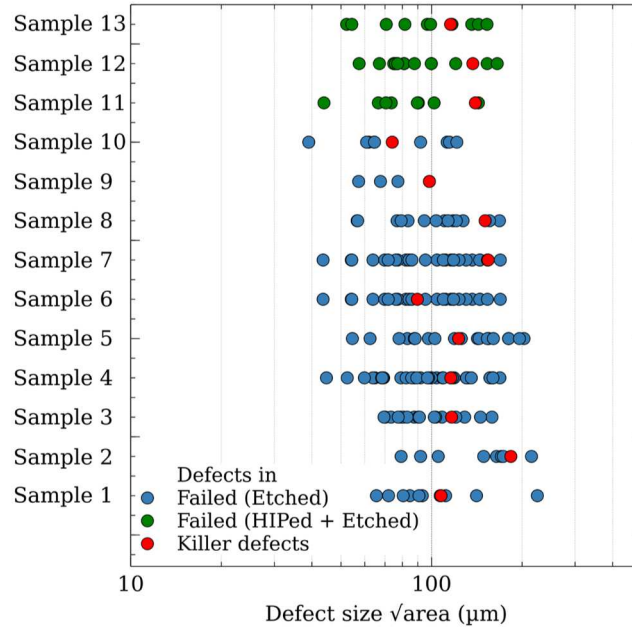


Figure 9. Rankings of the detected defects in broken chemically etched samples based on the \sqrt{area} parameter. Green and blue dots correspond to automatically detected defects in samples that respectively did and did not undergo a HIP treatment. Red dots correspond to killer defects leading to failure. \sqrt{area} is measured based on tomographic images.

Figure 10b and **Figure 10c** show respectively radial views of the killer and the largest defect before (dark gray) and after chemical etching (light gray). A comparison between **Figure 10b** and **Figure 10c** shows that : for the killer defect, a sharp root is observed (i.e. a small radius of curvature, ρ_c at the root of the defect) while the largest defect seems to exhibit a larger radius of curvature at its root: one could assume $\rho_c^{killer} \ll \rho_c^{largest}$. Assuming that notch-like defects can be idealized as elliptical notches with a root radius of curvature ρ and a depth a , the stress concentration (K_t) arising from those idealized elliptical notch defects can be estimated based on the classical following equation $K_t = 1 + 2\sqrt{a/\rho}$. The radius of curvature at the root of the elliptical notch is equal to b^2/a with b the opening (“thickness”) of the notch. Typical values of b and a measured on 2D radial projection of etched samples lead to $K_t = 5-8$. Thus even if the defect possesses a smaller projected area, it becomes the most harmful defect possibly due to a much smaller radius of curvature at its root. Prior to chemical etching, all defects are notch-like defects and exhibit large \sqrt{area} and a relatively sharp root. However, after chemical etching, the discrepancy between various notch-like defects increases dramatically as illustrated in **Figure 10b** and **Figure 10c**. It means that the efficiency of chemical etching may vary from a surface defect to another. This discrepancy is thought to be caused by the local variations of the density of chemical etchant in the neighborhood of the defect considered as shown by Lhuissier

et al. in [19]. Thus the sharpness of the defects subsequently to chemical etching is intimately linked to their shape in the as-built conditions as well as to the efficiency of chemical dissolution. This suggests that the most harmful surface defects in the as-built conditions may not remain as such after chemical etching. Note that this increased discrepancy can contribute to the larger scatter of the fatigue results observed when considering chemically etched samples with respect to as-built specimens.

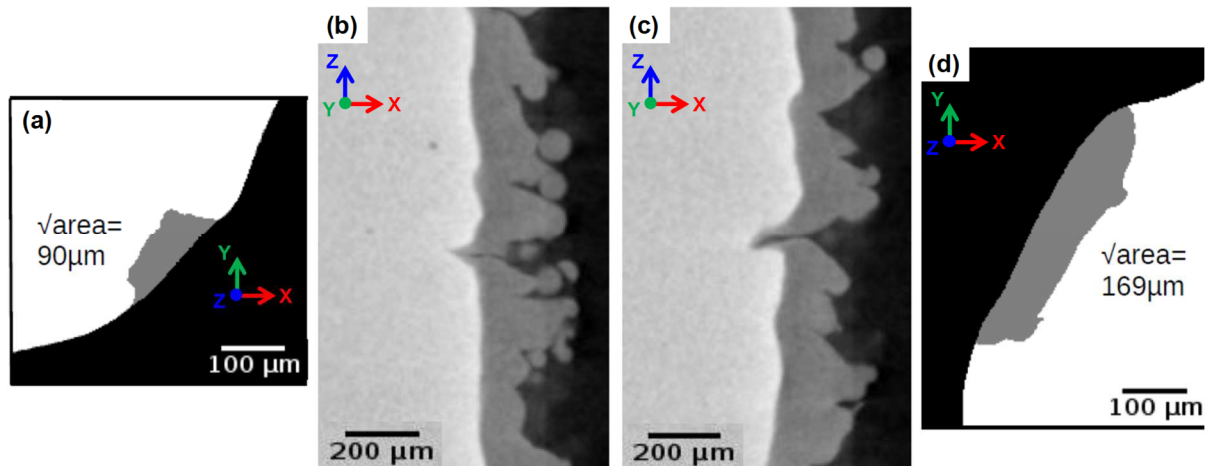


Figure 10. Comparison of the morphology of the killer defect (a, b) with the defect having the largest square root of the projected area (c, d) for a sample chemically etched (failure after $\approx 185\,000$ cycles at $\sigma_{max} = 295$ MPa, Sample 6 in **Figure 9**). (a, d) Average computation of the minimum and maximum local projections showing the square root of the projected area of the defects in gray. The corresponding values of $\sqrt{\text{area}}$ are indicated. (b, c) Radial views of both defects before (dark gray) and after chemical etching (light gray).

The fact that the defect responsible for fatigue failure is rarely the one with the largest $\sqrt{\text{area}}$ suggests that predictive tools such as *Kitagawa* diagrams should be modified to rely on a parameter that would give a better description of the surface defects including a stress concentration factor. The work of Tammis-Williams *et al.* [42] is particularly relevant to discuss this point because these authors looked at different ways of ranking defects for possible initiation sites. They proposed different ranking methods with an increased level of complexity including one based on Murakami equation (as done here) and others including stress concentration due to surface proximity, aspect ratio or proximity to other defects as well as plastic stress-strain concentration. Note that in our case the surface proximity factor is not relevant since the killer defect is always located at the surface. They found that the ranking method relying on the defect size is outperformed by more complex ranking method including for instance aspect ratio and stress heterogeneities. This is consistent with our results since we demonstrate that a description of the defect based on its projected area is not enough to capture the harmfulness of the surface defects. Finally, we would like to comment on our methodology since it suffers from several limitations that we should have in mind. The square root of the projected area of a killer defect identified based on microtomography was compared to the same defect characterized by SEM on the fracture surface. Small variations were detected, as exemplified by the comparison between **Figure 11a-b** and **Figure 11c-f**. Limited underestimation of the square root of the projected area measurement based on tomographic images is found, typically to be equal to about 5%. Such an error is therefore not expected to

strongly change the defect ranking based on the sole \sqrt{area} and shown in **Figure 9**. Thus one can consider that the determination of \sqrt{area} using microtomography projections is reliable. However, the exact morphology of the killer defect might not be fully captured using microtomography, at least with the voxel size used in the present work (2.5 μm). In particular, thin sharp defects with a small radius of curvature at its root are unlikely to be captured with the employed resolution, see **Figure 11**. Note that such defects can be seen as extreme situations. Once again this can play a key role for crack initiation because depending on the exact morphology of the defect, stress concentration might arise and cause fatigue crack initiation at defects which are not necessarily the largest ones based on the Murakami parameter (\sqrt{area}).

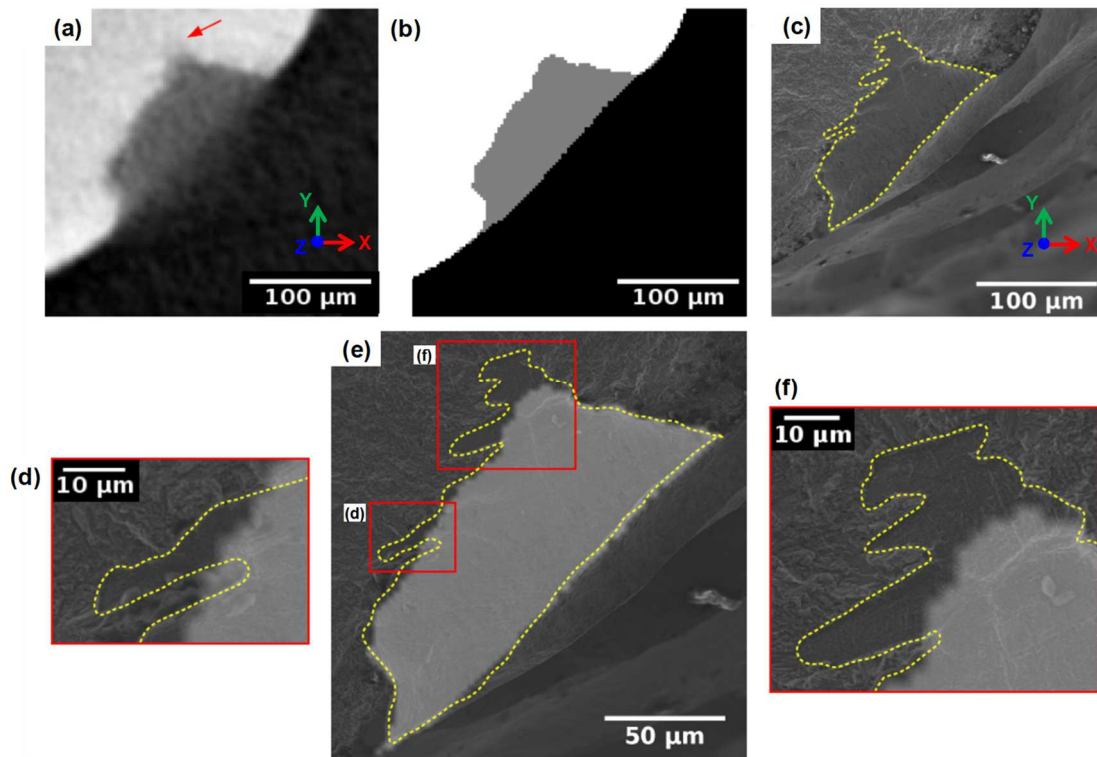


Figure 11. Comparison of the projected areas of the killer defect measured by laboratory X-ray tomography and SEM-SE micrograph on a sample chemically etched that failed after $\approx 185\,000$ cycles at $\sigma_{max} = 295$ MPa. (a) Minimum axial projection around the defect, the red arrow points out the region of crack initiation. (b) Average computation of the binarized minimum and maximum projections around the defect. (c) SEM micrograph of the defect on the fracture surface. (e) Overlap of the defect projected area obtained by X-ray tomography and SEM. (d, f) Higher magnification images of the overlap shown in (e). The dashed yellow line highlights the surface defect contour as detected by SEM.

6. Conclusion

The main conclusions of the present work can be drawn as follows.

- Chemical etching, a post-treatment suitable for complex geometries contrary to machining, brings a beneficial impact on the fatigue resistance of as-built EBM samples: the fatigue limit being increased by 50% and by nearly 100% when combined with a preliminary HIP-treatment.
- Fatigue failure of chemically etched samples is always caused by a residual notch-like defect at the surface and exceptionally by an internal defect brought at the surface through chemical etching (without HIP treatment).
- The developed methodology based on non-destructive inspections through X-ray microtomography prior to fatigue testing allows to consistently identify the killer defect in the population of the deepest notch-like defects. The killer defect is always found amongst this limited population of detected defects.
- **The current approach was applied to samples built by S-EBM but can be applicable to other AM-processing routes that are known to induce harmful surface defects.**
- Fatigue failure of chemically etched samples is reasonably well predicted relying on the classical *Kitagawa-Takahashi* diagram.
- Ranking defects based on \sqrt{area} is not enough to fully describe the harmfulness of notch like defects since the killer defect was rarely found as the largest one. This demonstrates that *Kitagawa-Takahashi* diagrams, largely used by the community must be used carefully.
- A limited error is made when relying on the measurement of \sqrt{area} using microtomography, about 5%. However, the exact morphology of the most harmful defects is not captured with the employed resolution. A parameter that includes the 3D defect morphology and its consequence on stress concentrations should be added to achieve more robust predictions.

Acknowledgements

The authors would like to thank the French “Agence Nationale de la Recherche (ANR)” and the French “Fondation de Recherche pour l’Aéronautique et l’Espace (FRAE)” for the financial support of this project entitled “Fabrication Additive et Fatigue de Structures Cellulaires Intégrées en Aéronautique” (FA2SCINAE-ANR-15-CE08-0038-03). This work was performed within the framework of the Center of Excellence of Multifunctional Architected Materials “CEMAM” n°AN-10-LABX-44-01 funded by the “Investments for the Future Program”.

References

- [1] B.P. Heintz, A. Rottmair, C. Körner, R.F. Singer, Cellular Titanium by Selective Electron Beam Melting, *Adv. Eng. Mater.* (2007) 360–364. doi:10.1002/adem.200700025.
- [2] E. Marin, S. Fusi, M. Pressacco, L. Paussa, L. Fedrizzi, Characterization of cellular solids in Ti6Al4V for orthopaedic implant applications : Trabecular titanium, *J. Mech. Behav. Biomed. Mater.* 3 (2010) 373–381. doi:10.1016/j.jmbbm.2010.02.001.
- [3] L.E. Murr, S.M. Gaytan, D.A. Ramirez, E. Martinez, J. Hernandez, K.N. Amato, P.W. Shindo, F.R. Medina, R.B. Wicker, Invited Review and Electron Beam Melting

- Technologies, *Mater. Sci. Technol.* 28 (2012) 1–14. doi:10.1016/S1005-0302(12)60016-4.
- [4] S.J. Li, L.E. Murr, X.Y. Cheng, Z.B. Zhang, Y.L. Hao, R. Yang, F. Medina, Compression fatigue behavior of Ti – 6Al – 4V mesh arrays fabricated by electron beam melting, 60 (2012) 793–802. doi:10.1016/j.actamat.2011.10.051.
- [5] T. Debroy, H.L. Wei, J.S. Zuback, T. Mukherjee, J.W. Elmer, J.O. Milewski, A.M. Beese, A. Wilson-heid, A. De, W. Zhang, Progress in Materials Science Additive manufacturing of metallic components – Process , structure and properties, *Prog. Mater. Sci.* 92 (2018) 112–224. doi:10.1016/j.pmatsci.2017.10.001.
- [6] J.J. Lewandowski, M. Seifi, Metal Additive Manufacturing: A Review of Mechanical Properties, *Annu. Rev. Mater. Res.* 46 (2016) 151–186. doi:10.1146/annurev-matsci-070115-032024.
- [7] M. Seifi, A. Salem, J. Beuth, O.L.A. Harrysson, J.J. Lewandowski, Overview of Materials Qualification Needs for Metal Additive Manufacturing, 68 (2016). doi:10.1007/s11837-015-1810-0.
- [8] ARCAM-AB, EBM-Hardware, (2015). <http://www.arcam.com/technology/electron-beam-melting/hardware/>.
- [9] S. Romano, A. Brückner-Foit, A. Brandão, J. Gumpinger, T. Ghidini, S. Beretta, Fatigue properties of AlSi10Mg obtained by additive manufacturing: Defect-based modelling and prediction of fatigue strength, *Eng. Fract. Mech.* 187 (2018) 165–189. doi:10.1016/j.engfracmech.2017.11.002.
- [10] A.H. Chern, P. Nandwana, T. Yuan, M.M. Kirka, R.R. Dehoff, P.K. Liaw, C.E. Duty, A review on the fatigue behavior of Ti-6Al-4V fabricated by electron beam melting additive manufacturing, *Int. J. Fatigue.* 119 (2019) 173–184. doi:10.1016/j.ijfatigue.2018.09.022.
- [11] H. Masuo, Y. Tanaka, S. Morokoshi, H. Yagura, T. Uchida, Y. Yamamoto, Y. Murakami, Influence of defects, surface roughness and HIP on the fatigue strength of Ti-6Al-4V manufactured by additive manufacturing, *Int. J. Fatigue.* 117 (2018) 163–179. doi:10.1016/j.ijfatigue.2018.07.020.
- [12] M. Kahlin, H. Ansell, J.J. Moverare, Fatigue behaviour of additive manufactured Ti6Al4V, with as-built surfaces, exposed to variable amplitude loading, *Int. J. Fatigue.* 103 (2017) 353–362. doi:10.1016/j.ijfatigue.2017.06.023.
- [13] T. Persenot, A. Burr, G. Martin, J.Y. Buffiere, R. Dendievel, E. Maire, Effect of build orientation on the fatigue properties of as-built Electron Beam Melted Ti-6Al-4V alloy, *Int. J. Fatigue.* 118 (2019) 65–76. doi:10.1016/j.ijfatigue.2018.08.006.
- [14] T. Persenot, J.-Y. Buffiere, E. Maire, R. Dendievel, G. Martin, Fatigue properties of EBM as-built and chemically etched thin parts, *Procedia Struct. Integr.* 7 (2017) 158–165. doi:10.1016/j.prostr.2017.11.073.
- [15] T. Persenot, A. Burr, E. Plancher, J. Bu, R. Dendievel, G. Martin, Effect of ultrasonic shot peening on the surface defects of thin struts built by electron beam melting : Consequences on fatigue resistance, 28 (2019) 821–830. doi:10.1016/j.addma.2019.06.014.
- [16] J. Damon, S. Dietrich, F. Vollert, J. Gibmeier, V. Schulze, Process dependent porosity and the influence of shot peening on porosity morphology regarding selective laser melted AlSi10Mg parts, *Addit. Manuf.* 20 (2018) 77–89. doi:10.1016/j.addma.2018.01.001.
- [17] N. Elad, S. Ramati, R. Shneck, N. Frage, O. Yeheskel, On the effect of shot-peening on fatigue resistance of AlSi10Mg specimens fabricated by additive manufacturing using selective laser melting (AM- SLM), *Addit. Manuf.* 21 (2018) 458–464. doi:10.1016/j.addma.2018.03.030.

- [18] S. Bagherifard, N. Beretta, S. Monti, M. Riccio, M. Bandini, M. Guagliano, On the fatigue strength enhancement of additive manufactured AlSi10Mg parts by mechanical and thermal post-processing, *Mater. Des.* 145 (2018) 28–41. doi:10.1016/j.matdes.2018.02.055.
- [19] P. Lhuissier, C. de Formanoir, G. Martin, R. Dendievel, S. Godet, Geometrical control of lattice structures produced by EBM through chemical etching: Investigations at the scale of individual struts, *Mater. Des.* 110 (2016) 485–493. doi:10.1016/j.matdes.2016.08.029.
- [20] C. de Formanoir, M. Suard, R. Dendievel, G. Martin, S. Godet, Improving the mechanical efficiency of electron beam melted titanium lattice structures by chemical etching, *Addit. Manuf.* 11 (2016) 71–76. doi:10.1016/j.addma.2016.05.001.
- [21] G. Pyka, G. Kerckhofs, I. Papantoniou, M. Speirs, J. Schrooten, M. Wevers, Surface Roughness and Morphology Customization of Additive Manufactured Open Porous Ti6Al4V Structures, (2013) 4737–4757. doi:10.3390/ma6104737.
- [22] B.G. Pyka, A. Burakowski, G. Kerckhofs, M. Moesen, S. Van Bael, J. Schrooten, M. Wevers, Surface Modification of Ti6Al4V Open Porous Structures Produced by Additive Manufacturing **, (2012) 363–370. doi:10.1002/adem.201100344.
- [23] Y. Murakami, Analysis of stress intensity factors of modes i, ii and iii for inclined surface cracks of arbitrary shape, *Eng. Fracture Mech.* 22 (1985) 101–114.
- [24] Y. Murakami, Material defects as the basis of fatigue design, *Int. J. Fatigue.* 41 (2012) 2–10. doi:10.1016/j.ijfatigue.2011.12.001.
- [25] T. Persenot, G. Martin, R. Dendievel, J.Y. Buffière, E. Maire, Enhancing the tensile properties of EBM as-built thin parts: Effect of HIP and chemical etching, *Mater. Charact.* 143 (2018) 82–93. doi:10.1016/j.matchar.2018.01.035.
- [26] M. Suard, G. Martin, P. Lhuissier, R. Dendievel, F. Vignat, J.J. Blandin, F. Villeneuve, Mechanical equivalent diameter of single struts for the stiffness prediction of lattice structures produced by Electron Beam Melting, *Addit. Manuf.* 8 (2015) 124–131. doi:10.1016/j.addma.2015.10.002.
- [27] U. Aecklid, M. Svensson, No Title, in: *Proc. Mater. Sci. Technol. Conf.*, Pittsburgh, 2019.
- [28] A. Du Plessis, I. Yadroitsava, I. Yadroitsev, Effects of defects on mechanical properties in metal additive manufacturing : A review focusing on X-ray tomography insights, *Mater. Des.* 187 (2020) 108385. doi:10.1016/j.matdes.2019.108385.
- [29] G. Meneghetti, D. Rigon, C. Gennari, An analysis of defects in fl uence on axial fatigue strength of maraging steel specimens produced by additive manufacturing, *Int. J. Fatigue.* 118 (2019) 54–64. doi:10.1016/j.ijfatigue.2018.08.034.
- [30] D. Greitemeier, F. Palm, F. Syassen, T. Melz, Fatigue performance of additive manufactured TiAl6V4 using electron and laser beam melting, *Int. J. Fatigue.* 94 (2017) 211–217. doi:10.1016/j.ijfatigue.2016.05.001.
- [31] D. Greitemeier, C. Dalle Donne, F. Syassen, J. Eufinger, T. Melz, Effect of surface roughness on fatigue performance of additive manufactured Ti–6Al–4V, *Mater. Sci. Technol.* 32 (2016) 629–634. doi:10.1179/1743284715Y.0000000053.
- [32] M. Seifi, M. Dahar, R. Aman, O. Harrysson, J. Beuth, J.J. Lewandowski, Evaluation of Orientation Dependence of Fracture Toughness and Fatigue Crack Propagation Behavior of As-Deposited ARCAM EBM Ti-6Al-4V, *Jom.* 67 (2015) 597–607. doi:10.1007/s11837-015-1298-7.
- [33] M. Seifi, A. Salem, D. Satko, J. Shaffer, J.J. Lewandowski, Defect distribution and microstructure heterogeneity effects on fracture resistance and fatigue behavior of EBM Ti–6Al–4V, *Int. J. Fatigue.* 94 (2017) 263–287. doi:10.1016/j.ijfatigue.2016.06.001.

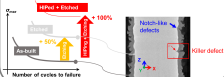
- [34] H. Galarraga, R.J. Warren, D.A. Lados, R.R. Dehoff, M.M. Kirka, Fatigue crack growth mechanisms at the microstructure scale in as-fabricated and heat treated Ti-6Al-4V ELI manufactured by electron beam melting (EBM), *Eng. Fract. Mech.* 176 (2017) 263–280. doi:10.1016/j.engfracmech.2017.03.024.
- [35] T. Persenot, Fatigue of Ti-6Al-4V thin parts made by Electron Beam Melting, Université de Lyon, 2018. <http://theses.insa-lyon.fr/publication/2018LYSEI117/these.pdf>.
- [36] U. Zerbst, M. Madia, B. Schork, J. Hensel, P. Kucharczyk, D. Ngoula, D. Tchuindjang, J. Bernhard, C. Beckmann, *Fatigue and Fracture of Weldments*, Springer, 2019.
- [37] M.. El Haddad, T.. Topper, K.. Smith, Prediction of non propagating cracks, *Eng. Fract. Mech.* 11 (1979) 573–584. doi:[https://doi.org/10.1016/0013-7944\(79\)90081-X](https://doi.org/10.1016/0013-7944(79)90081-X).
- [38] Y. Zhai, H. Galarraga, D.A. Lados, Microstructure, static properties, and fatigue crack growth mechanisms in Ti-6Al-4V fabricated by additive manufacturing: LENS and EBM, *Eng. Fail. Anal.* 69 (2016) 3–14. doi:10.1016/j.engfailanal.2016.05.036.
- [39] Y. Murakami, S. Kodama, S. Konuma, Quantitative evaluation of effects of non-metallic inclusions on fatigue strength of high strength steels. I: Basic fatigue mechanism and evaluation of correlation between the fatigue fracture stress and the size and location of non-metallic inclusions, *Int. J. Fatigue.* 11 (1989) 291–298. doi:10.1016/0142-1123(89)90054-6.
- [40] S. Beretta, S. Romano, A comparison of fatigue strength sensitivity to defects for materials manufactured by AM or traditional processes, *Int. J. Fatigue.* 94 (2017) 178–191. doi:10.1016/j.ijfatigue.2016.06.020.
- [41] M. Ciavarella, F. Monno, On the possible generalizations of the Kitagawa-Takahashi diagram and of the El Haddad equation to finite life, *Int. J. Fatigue.* 28 (2006) 1826–1837. doi:10.1016/j.ijfatigue.2005.12.001.
- [42] S. Tamma-Williams, P.J. Withers, I. Todd, P.B. Prangnell, The Influence of Porosity on Fatigue Crack Initiation in Additively Manufactured Titanium Components, *Sci. Rep.* 7 (2017). doi:10.1038/s41598-017-06504-5.

EXPERIMENTS

S-N curves

X-ray microtomography

SEM



PREDICTIONS

Detection of notch-like defects

Kitagawa-Takahashi diagrams

